Arch. Metall. Mater. **71** (2026), 1, 173-186

DOI: https://doi.org/10.24425/amm.2026.157779

D. MARIAPPAN[1*], P. SIVALINGAM[1]

WIRE ARC ADDITIVE MANUFACTURING OF SS321 USING COLD METAL TRANSFER: RSM-BASED PROCESS OPTIMIZATION AND TENSILE CHARACTERIZATION

Wire arc additive manufacturing (WAAM) has emerged as a promising technology for producing complex, large-scale components with high material deposition rates, reduced waste, and shorter lead times. This study focused on optimizing process parameters in cold metal transfer (CMT)-based WAAM to achieve superior bead geometry and enhanced microhardness in stainless steel 321. Welding current, travel speed, and shielding gas mixture ratio were selected as input parameters, whereas bead width, depth of penetration, diffusion area, and microhardness were the response variables. Using response surface methodology (RSM) with a central composite design, a regression model was developed to identify optimal process parameters. The optimal parameters are 150 A current, 4-5 mm/s travel speed, and 0-10% CO_2 shielding gas, which produced favorable bead geometry and a microhardness of 180 HV, validating the RSM model's predictive accuracy. Experimental validation confirmed the model's accuracy in producing high-quality SS321 structures. Tensile testing validated mechanical performance, with yield strength 372.07-384.46 MPa, ultimate tensile strength (UTS) 590.19-598.96 MPa, and elongation 38% (90°) and 41% (0°), surpassing ASTM A240/A240M-20a standards. Scanning electron microscopy fractography revealed ductile failure with micro-voids and fine dimples, confirming a ductile mode of mechanical behavior. These findings demonstrate the reliability of RSM in optimizing CMT-WAAM processes and additive manufacturing applications.

Keywords: WAAM; CMT; SS321; Bead geometry; Optimization; RSM

1. Introduction

Conventional manufacturing techniques such as casting, machining, and welding often involve multiple secondary operations, resulting in increased energy consumption and production costs [1]. In contrast, additive manufacturing (AM) allows for efficient fabrication of complex, near-net-shape components with reduced material waste and shorter processing times [2]. Wire and arc additive manufacturing (WAAM), a prominent AM technique, uses arc-based welding processes such as gas metal arc welding (GMAW), gas tungsten arc welding (GTAW), and plasma arc welding (PAW) to deposit material layer by layer [3,4]. Among these, GMAW is widely preferred due to its deposition rate, which is typically 2-3 times higher than that of GTAW and PAW [5]. A variant of CMT developed by Fronius in 2004, enables precise material deposition with significantly reduced heat input [6]. The process features a reciprocating wire feed mechanism and electronically synchronized arc phases, which reduce spatter and distortion, improving weld quality, particularly for thin or heat-sensitive materials [7].

Stainless steel 321 (SS321), a titanium-stabilized austenitic stainless-steel alloy containing approximately 18% Cr and 10-15% Ni, is known for its excellent weldability, mechanical strength, and resistance to intergranular corrosion at elevated temperatures (900-1450°C) [8]. Its thermal and corrosion resistance make it a cost-effective alternative to superalloys for demanding applications in aviation, nuclear reactors, oil refineries, heat exchangers, chemical processing units, and automotive exhaust systems [9]. These attributes also render SS321 highly suitable for advanced manufacturing processes such as WAAM, where precise control over mechanical and microstructural properties is crucial. In CMT-based WAAM, optimization of process parameters is critical for achieving desirable bead geometry, mechanical properties, and structural integrity.

Recent studies on GMAW-based WAAM of AISI 321 stainless steel highlight its ability to produce complex components with controlled heat input and stable properties. Wang et al. [9] used CMT-WAAM to fabricate multilayer SS321 with austenitic-ferritic microstructure, uniform hardness, and superior corrosion resistance to wrought alloy. Prakash et al. [23] observed

[1] DEPARTMENT OF ROBOTICS AND AUTOMATION ENGINEERING, PSG COLLEGE OF TECHNOLOGY, COIMBATORE- 641004, TAMIL NADU, INDIA

* Corresponding author: dhanabalk91@gmail.com

3.6-5.9 FN ferrite with comparable hardness but slightly lower toughness due to δ-ferrite. Kumar et al. [22] reported higher room-temperature strength, reduced high-temperature ductility, and adherent spinel oxides following parabolic oxidation kinetics. Overall, these studies confirm GMAW-WAAM's suitability for SS321 with consistent microstructure and mechanical performance.

Several studies have investigated the mechanical and microstructural characteristics of WAAM-fabricated structures across various materials. Qiu et al. [10] used GTAW-WAAM to fabricate C276 wall structures, reporting enhanced microhardness and tensile strength (469 ± 52 MPa), though with reduced ductility attributed to microstructural anisotropy. Dinovitzer et al. [11] observed defects such as humping and undercutting in TIG-based WAAM of Hastelloy, linking these to thermocapillary effects and weld pool instability. Yamaguchi et al. [12] examined the influence of shielding gases on surface roughness in GMAW-based WAAM, noting that argon improved surface finish during short-circuiting, while CO_2 increased droplet formation due to elevated heat input. Rajeev et al. [13] investigated Stellite 6 deposition on AISI H13 steel using the CMT process, demonstrating that correcting arc length reduced dilution and lower heat input enhanced hardness and refined the microstructure.

Various optimization strategies have proven effective in refining arc welding processes. For example, Pavan et al. [14] used response surface methodology (RSM) to evaluate shielding gas mixtures in A-TIG welding of 316L stainless steel, observing better penetration with helium-based gases at lower heat input compared to argon, despite helium's higher cost and limited industrial availability. Mohan et al. [15] applied Taguchi-based grey relational analysis to maximize penetration in nuclear-grade stainless steel, demonstrating significant improvements in performance. Similarly, Kolahan and Heidari [16] used Taguchi's method to construct regression models correlating GMAW parameters with output responses, providing a robust predictive framework. Sivasakthivel and Sudhakaran [17] developed a neural network model to predict bead geometry during GMAW of preheated stainless steel, achieving an error margin below 4%, and established empirical regression equations for optimization.

Despite these advancements, the influence of shielding gas ratio on CMT-based WAAM of SS321 remains largely unexplored. This study investigates the effects of welding current, travel speed, and shielding gas ratio on arc characteristics, penetration depth, bead profile, and microhardness through single-track bead-on-plate experiments conducted on SS321 substrates, providing a foundation for producing distortion-free thin-wall structures. To systematically optimize these process parameters and understand their combined influence on bead geometry and microhardness. RSM enables efficient experimental design, identifies significant linear, quadratic, and interaction effects, and develops predictive models for process optimization in CMT-WAAM. The findings offer insights into minimizing material waste and energy consumption while identifying optimal conditions for fabricating SS321 thin-wall structures with enhanced microhardness and structural integrity, thereby advancing the application of CMT-WAAM in high-performance and nuclear-grade components.

2. Experimental procedure

Single-track welding of austenitic stainless steel 321 (SS321) was performed using a robotically controlled CMT-based GMAW process. SS321 plates measuring 150×120×6 mm^3 served as substrates, whereas ER321 filler wire with a diameter of 1.2 mm was used for deposition. The chemical compositions of both the base and filler materials were determined using an optical emission spectrometer, and the results are listed in TABLE 1. Before to welding, the substrates were cleaned with acetone and securely clamped on a welding fixture. A six-axis Fanuc Arc Mate 100iC robotic arm was used to control the welding torch, while the CMT process was powered by a Fronius TPS 400i power source. The experimental setup is illustrated in Fig. 1.

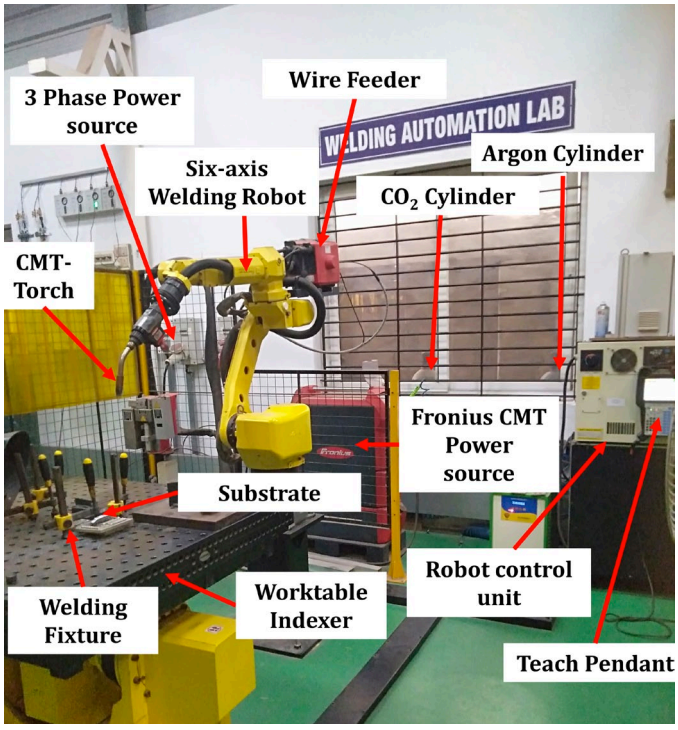

Fig. 1. CMT-based WAAM setup used for single-track analysis of ER321 wire

TABLE 1

Chemical compositions of SS321 substrate and ER321 filler wire (wt.%)

Element	C	Si	Mn	P	S	Cr	Ni	Mo	Cu	V	Ti	Cu	Fe
SS321	0.051	0.475	1.04	0.033	0.005	17.63	9.170	0.419	0.374	0.091	0.298	0.125	70.1
ER321	0.049	0.50	1.47	0.024	0.02	17.05	9.10	0.46	0.15	0.087	0.356	0.15	70.58

The Fronius CMT welding power source was integrated with a robotic manipulator, allowing for pre-programmed motion and precise control of welding parameters via the robot controller's teach pendant. A proportional gas mixing unit, supported by Flow Vision graphical software, was used to accurately regulate shielding gas mixture ratios. Preliminary single-track welding trials were performed using ER321 filler wire on SS321 substrates, as shown in Fig. 2. Key WAAM process parameters including welding current, travel speed, and shielding gas composition were selected based on a literature review and AWS standards. These trials established suitable parameter ranges for developing an experimental design matrix using the RSM approach.

2.1. Sample preparations

Single-track bead-on-plate weldments were carried out on ER321, and cross-sectional specimens ($20\times5\times6$ mm^3) were extracted using wire electrical discharge machining shown in Fig. 2. The samples were cold-mounted with acrylic resin and prepared using standard metallographic procedures involving grinding with SiC papers (80-2000 grit) and polishing to achieve a mirror finish. Spectroscopic microscopy was used to capture images of the prepared surfaces, which were analyzed using ImageJ software to measure bead width (BW), depth of penetration (DOP), and diffusion area (DA) after converting pixel data to millimeters. Microhardness testing was performed on the same cross-sections using a Vickers microhardness testing standard ASTM E384-17 with a 500 g load and 15 s dwell time, and the average of three indentations made in the fusion zone was used to evaluate the effect of process parameters. Tensile tests were conducted on specimens extracted from the SS321 WAAM thin wall in accordance with ASTM E8 standards and scanning electron microscopy (SEM) is used find the fracture morphology of tensile samples.

3. Development of experimental design matrix

The process parameters and their ranges were determined based on pilot track trials are listed in TABLE 2. Literature surveys and AWS standards were used to fix certain crucial WAAM parameters, as shown in TABLE 3. The CMT-based WAAM process parameters influencing bead geometry and hardness included welding current (A), travel speed (mm/s), and the shielding gas mixture (Ar%:CO_2%). A three-factor, 3-level central composite design (CCD) was used to structure the experiments, resulting in 20 trials: 8 corresponding to the cube points, 6 to the star points, and 6 to the center points. The process parameters were coded with values ranging from –1 to +1, corresponding to the lower and upper limits, with equal intervals between these extremes. The formula used to calculate intermediate coded values is shown in Eq. (1):

$$X_i = 2X - \frac{X_{\max} + X_{\min}}{X_{\max} - X_{\min}} \tag{1}$$

A design of experiments (DOE) was developed using an RSM-based CCD matrix set at a 95% confidence level. On the basis of DOE, single-track trials were conducted using SS321 wire to evaluate bead profiles, including bead width (mm), DOP(mm), diffusion area (mm^2), and microhardness ($HV_{0.5}$). After the trials, bead geometries were examined using an Dewinter-optima Spectro microscope. The images obtained were subsequently analyzed with ImageJ software for precise measurements of key parameters such as bead width, DOP, and diffusion area, is illustrated in Fig. 3.

TABLE 2

Process Parameter and their Ranges

Factor	Variable	Units	Levels of variables		
			–1	0	+1
A	Current	A	130	150	170
B	Travel Speed	mm/sec	4	5	6
C	CO_2 range	%	0	10	20

* Argon gas as Primary gas mixture

TABLE 3

Fixed WAAM process parameters

Arc length	0.5 mm
Gas flow rate	15 l/min
Torch angle	90°
Standoff distance	13 mm

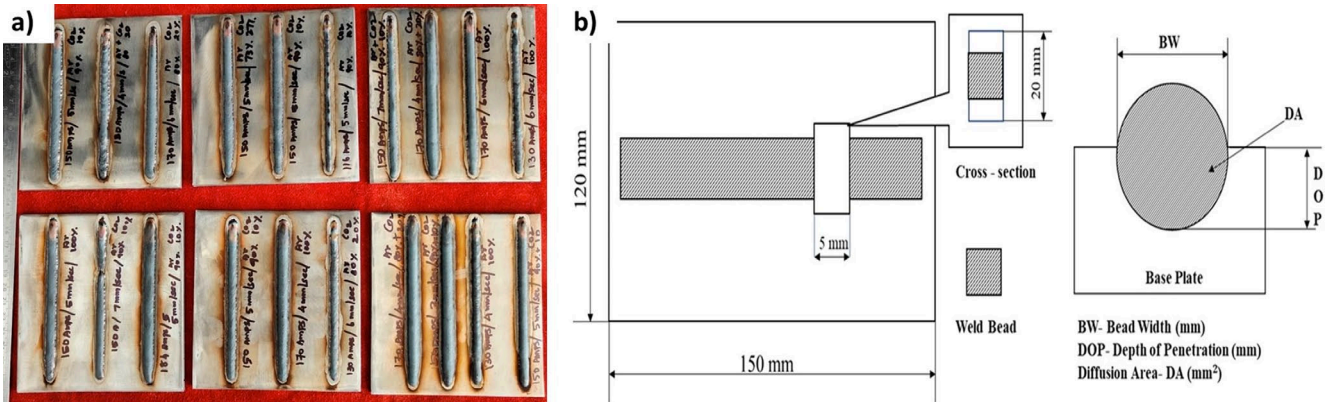

Fig. 2. (a) Single-track bead-on-plate deposition of ER321 wire on an SS321 substrate; (b) schematic representation of the cross-sectional bead profile

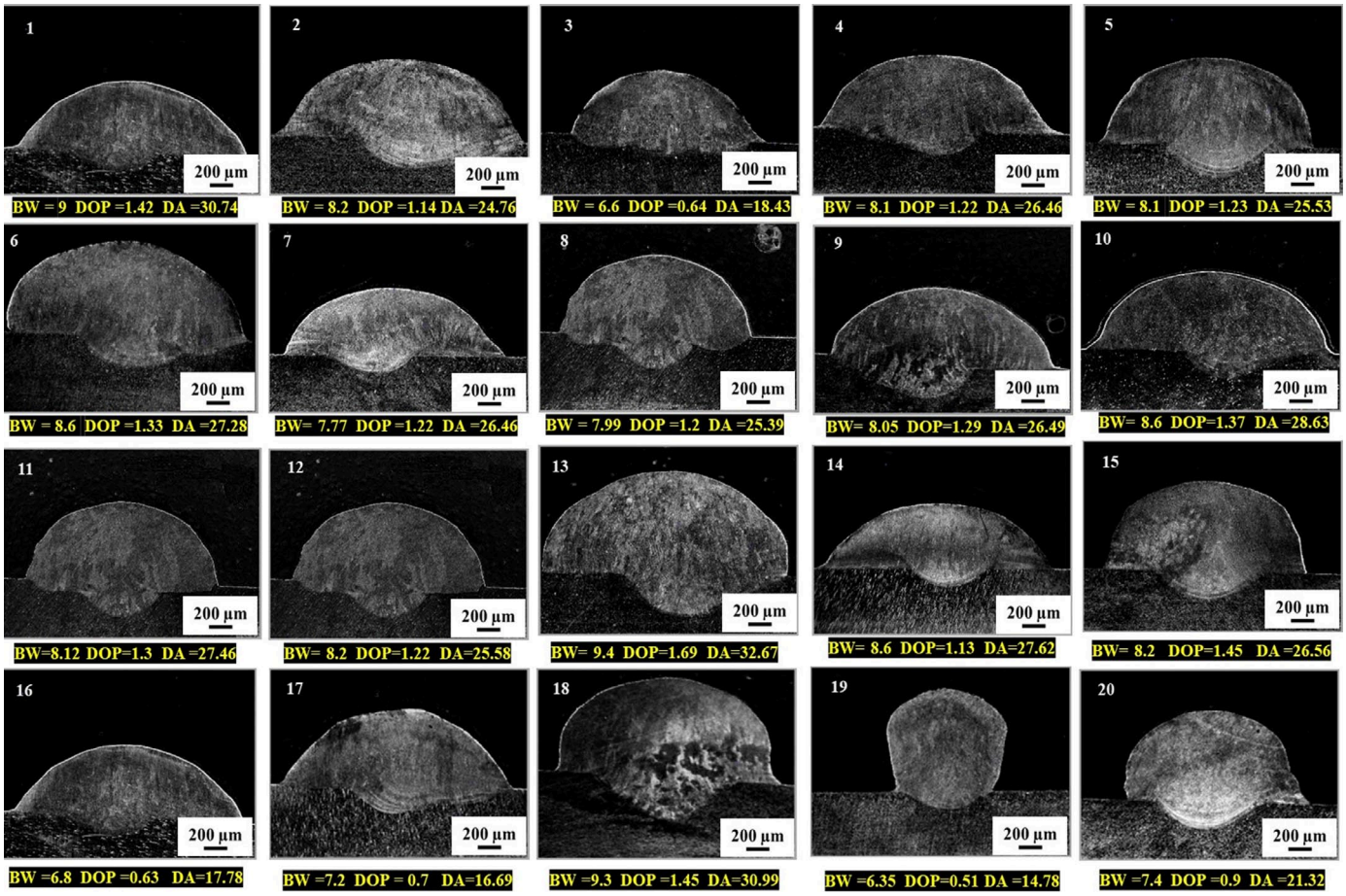

Fig. 3. Macrographs for measuring the bead geometry according to the experimental design matrix

TABLE 4

Experimental Design Matrix

S. No	Welding Current (A)	Travel Speed (mm/s)	CO_2 Gas (%)	Bead Width (mm)	DOP (mm)	Diffusion Area (mm^2)	Micro-hardness (HV)
1.	170	5	10	9	1.42	30.74	212
2.	150	5	0	8.2	1.14	24.76	180
3.	130	6	20	6.6	0.64	18.43	170
4.	150	5	10	8.1	1.22	26.46	174
5.	150	5	10	8.1	1.23	25.53	175
6.	150	4	10	8.6	1.33	27.82	176
7.	150	6	10	7.77	1.12	23.95	173
8.	150	5	10	7.99	1.2	25.39	175
9.	150	5	10	8.05	1.29	26.49	176
10.	170	6	20	8.6	1.37	28.63	202
11.	150	5	10	8.12	1.3	27.46	176
12.	150	5	10	8.2	1.22	25.58	174
13.	170	4	20	9.4	1.69	32.67	211
14.	170	6	0	8.6	1.13	27.62	212
15.	150	5	20	8.2	1.45	26.56	174
16.	130	5	10	6.8	0.63	17.78	171
17.	130	4	0	7.2	0.7	16.69	172
18.	170	4	0	9.3	1.45	30.99	223
19.	130	6	0	6.35	0.51	14.78	173
20.	130	4	20	7.4	0.9	21.32	169

3.1. Development of regression models

A second-order quadratic regression model was formulated to establish the relationship between process parameters and output responses for the SS321 single-track layer. In this model, the response (Y) is expressed as a function of the CMT-WAAM process parameters, as shown in Eq. (2):

$$Y = f(A, B, C) \tag{2}$$

The detailed form of the second-order regression equation describing the response (Y) is presented in Eq. (3):

$$Y = B_0 + n\sum_{i=1} B_1 X_i \left(\sum_{i=1}^{n} B_i X_i \right)^2 + \sum_{i=1}^{n-1} \sum_{j=0}^{n} B_{ij} X_j \tag{3}$$

In this equation, Y denotes the response variable, B_0 represents the average response, and X_i and X_j are the coded independent variables. The term B_i indicates the linear coefficients, B_{ii} refers to the quadratic coefficients, and B_{ij} signifies the interaction coefficients specific to the SS321 welded single track.

A second-order polynomial regression model was formulated to define the empirical relationship between the responses and the parameters of the CMT-GMAW welding process. This relationship is expressed in Eq. (4).

$$\begin{aligned} Y = B_0 + &B_1\ (\text{Welding Current}) + B_2\ (\text{Travel Speed}) + \\ &B_3\ (\text{Gas Mixture}) + B_4\ (\text{Welding Current} \times \text{Travel Speed}) + \\ &B_5\ (\text{Welding Current} \times \text{Gas Mixture}) + B_6\ (\text{Travel Speed} \times \\ &\text{Gas Mixture}) + B_7\ (\text{Welding Current})^2 + \\ &B_8\ (\text{Travel Speed})^2 + B_9\ (\text{Gas Mixture})^2 \end{aligned} \tag{4}$$

3.2. Coded Equations

Design-Expert v23.1.6 was used to develop second-order regression models for bead width, penetration, diffusion area, and microhardness, identifying significant coefficients at 95% confidence. Positive and negative coefficients indicate synergistic and antagonistic effects, respectively, as represented in Eq. (5)-(8).

$$\begin{aligned} \text{Bead Width (mm)} = &+ 8.12 + 1.06\,A - 0.3980\,B + \\ &0.0550\,C + 0.0187\,A \times B - 0.0438\,A \times C\ 0.0063\,B \times \\ &C - 0.2541\,A^2 + 0.0309\,B^2 + 0.0459\,C^2 \end{aligned} \tag{5}$$

$$\begin{aligned} \text{DOP (mm)} = &+ 1.24 + 0.3680\,A - 0.1300\,B + \\ &0.1120\,C - 0.0237\,A \times B + 0.0187\,A \times C \\ &- 0.0087\,\text{B} \times C - 0.2218\,A^2 - 0.0218\,B^2 + 0.0482\,C^2 \end{aligned} \tag{6}$$

$$\begin{aligned} \text{Diffusion Area (mm}^2\text{)} = &+ 26.10 + 6.16\,A - 1.61\,B + \\ &1.28\,C - 0.3262\,A \times B - 0.6987\,A \times C - \\ &0.2062\,B \times C - 1.75\,A^2 - 0.1250\,B^2 - 0.3500\,C^2 \end{aligned} \tag{7}$$

$$\begin{aligned} \text{Microhardness (HV)} = &+ 175.22 + 20.50\,A - \\ &2.10\,B - 3.40\,C - 2.75\,A \times B - 2.00\,A \times C + \\ &0.2500\,B \times C + 15.95\,A^2 - 1.05\,B^2 + 1.45\,\text{C}^2 \end{aligned} \tag{8}$$

4. Analysis of variance

Analysis of variance (ANOVA) was conducted to assess the statistical significance of the developed RSM models and to evaluate the influence of welding parameters on bead width, penetration depth, diffusion area, and microhardness in SS321 single-track bead-on-plate weldments. The significance of each model coefficient was determined based on p-values (<0.05), as summarized in TABLE 5. High F-values of 271.99 (bead width), 121.19 (penetration), 119.71 (diffusion area), and 946.00 (microhardness) indicate strong model validity. Bead width was significantly influenced by factors A, B, C, and A^2, with a predicted R^2 of 0.9807 and an adjusted R^2 of 0.9923. Penetration depth was governed by A, B, C, and A^2, with predicted and adjusted R^2 values of 0.9537 and 0.9827, respectively. For diffusion area, significant terms included A, B, C, AC, and A^2, with a predicted R^2 of 0.9747 and an adjusted R^2 of 0.9825. Microhardness was significantly affected by A, B, C, AB, AC, A^2, and C^2, with R^2 values of 0.9946 (predicted) and 0.9978 (adjusted). All models showed a non-significant lack of fit, confirming their reliability for predicting CMT-WAAM process responses in SS321.

The residuals, representing the differences between experimental and RSM-predicted values, were analyzed using normal probability plots. The derived equations reliably predict bead width, penetration depth, diffusion area, and microhardness in SS321 weldments. Validation tests showed strong agreement between experimental and predicted values. Fig. 4(a)-(d) illustrates this correlation, affirming the accuracy of the RSM models.

4.1. 3D Response Surface Modeling of Individual Process Responses

The interaction between two parameters was examined while keeping the third parameter fixed at its central level. Fig. 5(a)-(c) illustrates the effects of the parameters on bead width, analyzed through surface response plots. Fig. 5(a) shows

TABLE 5

Summary of ANOVA results for all responses

Response	Sum of Squares (Reg.)	Sum of Squares (Res.)	DF (Reg.)	DF (Res.)	Mean Square (Reg.)	Mean Square (Res.)	F-Value	P-Value	R^2 (%)	Adj. R^2 (%)
Bead Width	12.99	0.0531	9	10	1.44	0.0053	271.99	0.0001	99.59	99.23
Penetration	1.88	0.0172	9	10	0.2084	0.0017	121.19	0.0001	99.09	98.27
Dilution Area	448.59	4.16	9	10	49.84	0.4164	119.71	0.0001	99.08	98.25
Microhardness	5774.02	6.78	9	10	641.56	0.6782	946.00	0.0001	99.88	99.78

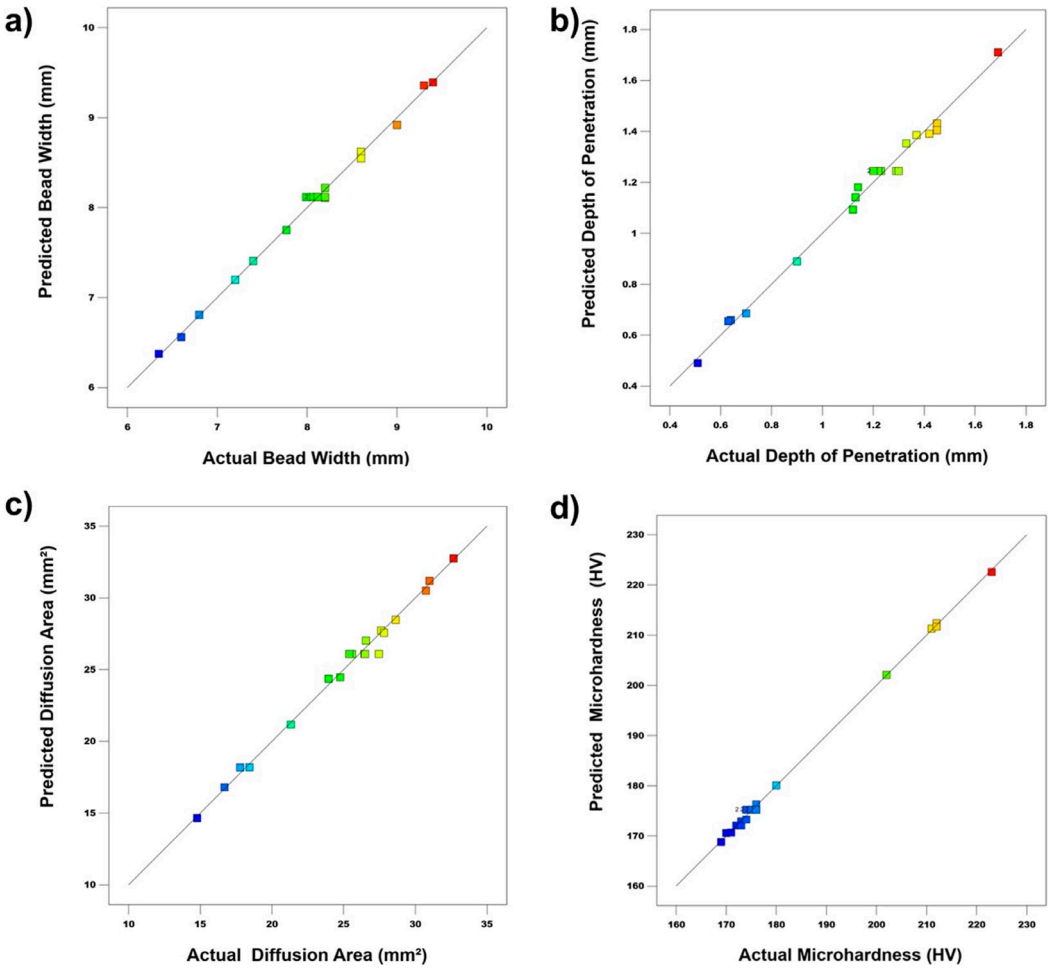

Fig. 4. Experimental vs Predicted graph of all responses

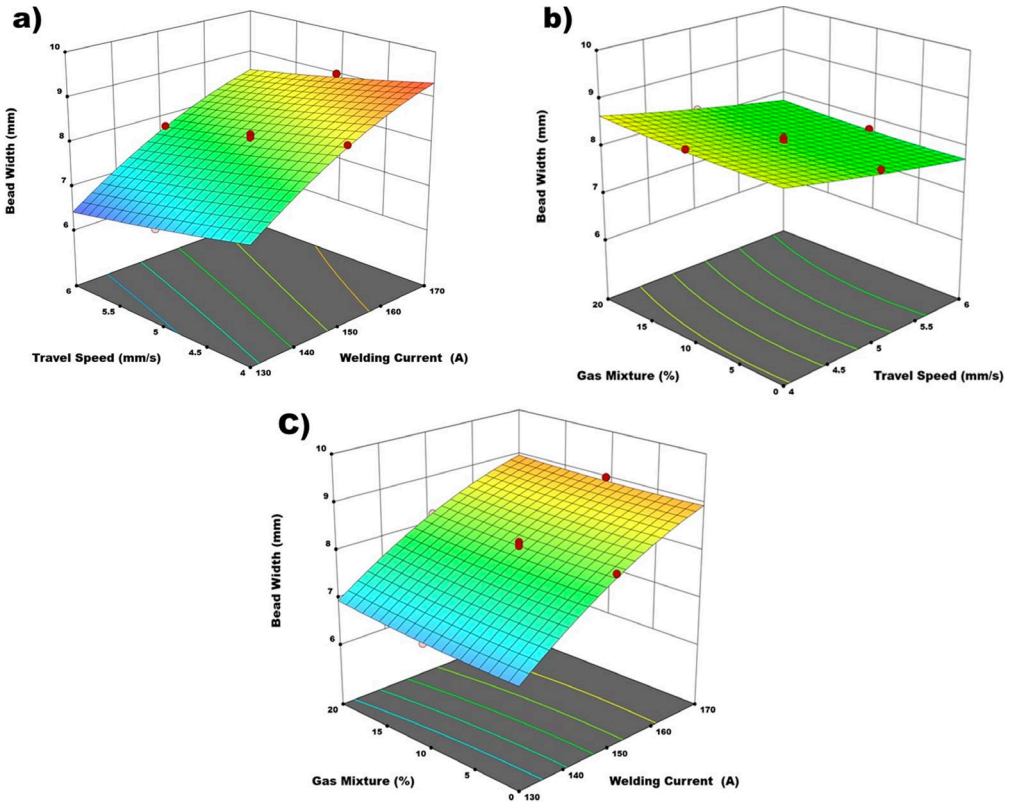

Fig. 5. 3D Response surface plots for bead width

that both welding current and travel speed directly influence bead width. As welding current increases and travel speed decreases, bead width gradually increases due to higher heat input, which enhances bead formation.

Conversely, as travel speed increases, bead width decreases because of reduced heat input and lower metal deposition on the substrate. Fig. 5(b) indicates that the interaction between travel speed and gas mixture percentage does not significantly affect bead width. Fig. 5(c) reveals the relationship between welding current and gas mixture percentage. At elevated welding currents, bead width increases with a higher CO_2 gas mixture percentage.

Surface response plots, shown in Fig. 6(a)-(c), were used to analyze the relationships between process parameters affecting the DOP. Fig. 6(a) illustrates the interaction between current and travel speed, showing that DOP decreases with lower current and higher travel speed. A higher current combined with lower travel speed increases heat flux, thereby enhancing substrate penetration. Fig. 6(b) shows the effect of gas mixture percentage and travel speed on DOP. Increasing travel speed reduces the heat supply per unit length of the bead, leading to a lo-wer DOP.

Conversely, lower travel speed increases DOP when paired with high current. Fig. 6(c) depicts the relationship between gas mixture percentage and welding current. As welding current increases, DOP improves due to the influence of the shielding gas mixture. A gas mixture of 20% CO_2 results in slightly higher DOP compared to pure argon. Although pure argon provides excellent arc stability, minimal oxidation, and a smooth surface, the CO_2 mixture enhances penetration in this context, as shown in the surface plots.

Fig. 7(a) demonstrates, that lower welding current and travel speed lead to reduced material deposition, as indicated by narrower bead width and DOP. Higher current and lower speed increase the diffusion area, which is also influenced by variations in shielding gas that affect arc characteristics and heat transfer. Both bead width and DOP increase with higher energy input. Fig. 7(b) indicates that travel speed and gas mixture percentage have minimal impact on the diffusion area under the tested conditions. Fig. 7(c) shows that the diffusion area rises with welding current and gas mixture percentage, peaking at 170 A. RSM predictions, based on 150 A, 4 mm/s, and 10% CO_2, show minimal changes in diffusion area with varying CO_2 percentages (0%, 10%, 20%) at 150 A and 5 mm/s.

Similarly, Fig. 8(a)-(c) illustrates how input parameters affect microhardness in the single-layer bead geometry of SS321. Fig. 8(a) shows that at lower welding currents, microhardness improves slightly with varying travel speeds due to stable arc characteristics and heat input, which stabilize cooling rates and hardness. Fig. 8(b) shows that travel speed and gas mixture have a minimal impact on microhardness, as indicated by the flat surface plot. Fig. 8(c) reveals that at 150 A welding current, microhardness remains stable across different travel speeds with 10% and 20% CO_2 shielding gas. At lower currents and higher travel speeds, reduced heat input results in faster cooling, finer grains, and slightly increased hardness in the SS321 single-track layer.

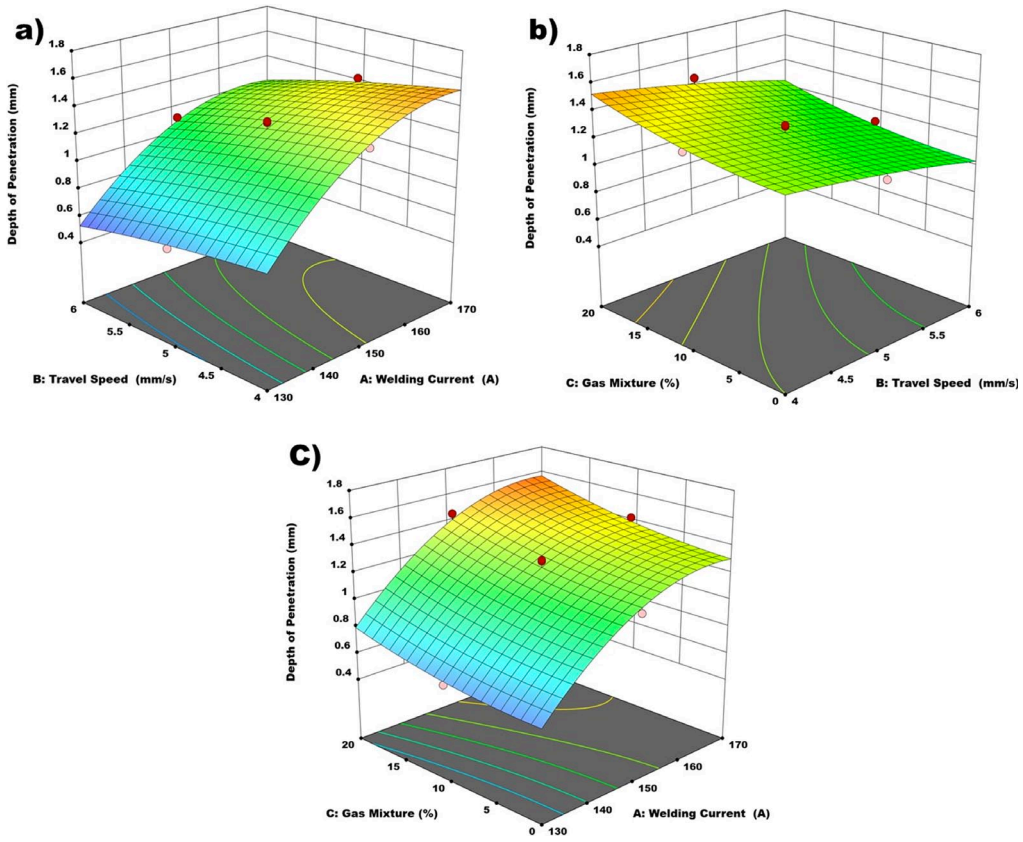

Fig. 6. 3D Response surface plots for depth of penetration

Microhardness peaks at 223 HV with a current of 170 A, a travel speed of 4 mm/s, and pure argon (Ar). At higher currents, with 10% and 20% CO_2 gas mixtures, the difference in hardness is minimal. Increased material deposition due to high current and low travel speed, combined with high heat flux density from CO_2 mixtures, enhances bead width and DOP. Pure argon offers better arc stability, a uniform bead profile, lower surface roughness, and improved hardness for SS321.

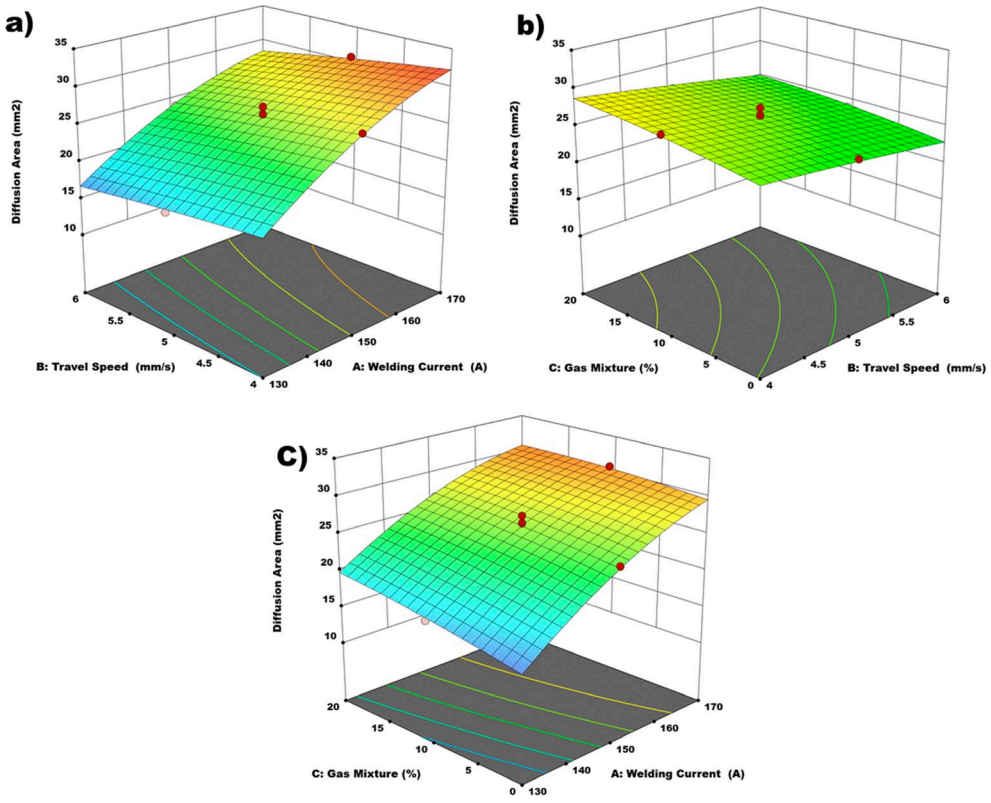

Fig. 7. 3D Response surface plots for diffusion area

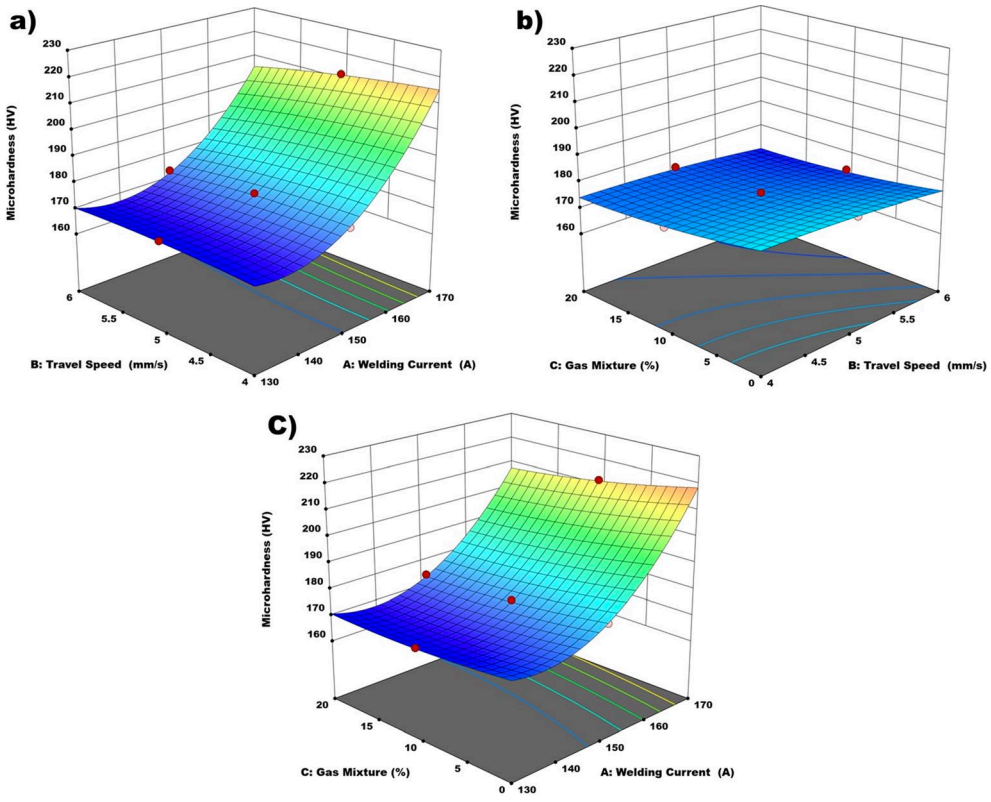

Fig. 8. 3D Response surface plots for microhardness

5. Results and discussion

5.1. Influence of welding current

Welding current significantly influences bead geometry and weld quality by increasing heat input, resulting in a larger melt pool, wider bead, and deeper penetration [9,18,19]. At low travel speeds, bead width initially increases but may later decrease due to sagging, with minimal effects on dilution and hardness [20]. As shown in the 3D response surface plots (Figs. 4-7), increasing current enhances bead width, penetration depth, and diffusion area. However, excessive current can lead to an overly convex bead and reduced penetration, compromising weld quality [21]. Microstructural observations of the first SS321 layer in WAAM revealed fine equiaxed dendrites with minimal ferrite, contributing to higher microhardness [22,23]. Experimental results (Fig. 3) confirm that both bead geometry and microhardness increase with current. The optimum parameters identified through RSM confirm their reliability for high-quality SS321 WAAM builds.

5.2. Influence of Travel Speed

Welding travel speed critically influences bead geometry and microhardness by altering heat input and deposition rate [9]. Higher speeds reduce the deposited metal volume per unit length, producing narrower beads with reduced penetration and faster solidification [21,24]. Maximum penetration is typically achieved at lower speeds, regardless of current, indicating a stronger influence of travel speed [25]. Intermediate speeds promote refined microstructures in the coarse-grained heat-affected zone, enhancing hardness [26]. Abioye et al. [27] also reported that lower speeds increase Cr and Ni content, which improve hardness by stabilizing austenite and enhancing corrosion resistance.

Additionally, bead-on-plate experiments on SS321 demonstrate that travel speed significantly influences bead geometry as well as mechanical and microstructural properties. Macrographs shown in Fig. 3. illustrate variations in bead width, penetration depth, and diffusion according to travel speed, as detailed in TABLE 4. The results, supported by 3D response plots (Figs. 4-7), reveal that higher travel speeds result in lower bead profiles and microhardness. At travel speeds of 4 and 5 mm/s with various welding currents, uniform bead geometry and stable microhardness values are observed at 150A. Notably, the highest bead geometry and microhardness of 223 HV are achieved at 170 A and 4 mm/s for SS321 bead-on-plate weldments.

5.3. Influence of Shielding Gases

Shielding gases protect the weld pool from atmospheric contamination and influence arc stability and weld quality [28]. Pure argon provides a stable, narrow arc and reduces surface irregularities, resulting in higher hardness without the formation of scatter [9]. In contrast, CO_2 is more economical and enhances thermal conductivity, increasing heat input and penetration depth [29]. Liao and chen. [30] observed that higher CO_2 content promotes dendritic microstructures, with coarser dendrites at increased levels. Both dendritic and lathy ferrite morphologies form due to peritectic solidification and ferrite transformation during cooling [31]. Although increased ferrite content can enhance hardness, higher CO_2 levels tend to reduce the overall hardness of the weld metal [32].

The experimental design for single-track bead-on-plate weldments with SS321 demonstrates that shielding gas mixtures exert a significant impact on bead geometry and hardness (see TABLE 4). Higher CO_2 concentrations increase bead width and penetration depth, as shown in (Figs. 4-7) and the cross-sectional measurements in Fig. 3. Hardness decreases with higher CO_2 but improves with pure argon or a 10% CO_2 mixture. The GMAW-CMT method effectively addresses spattering and arc instability. For thin WAAM structures, the optimal parameters are pure argon shielding gas, 150 A current, and a travel speed of 5 mm/s, which achieve the desired bead geometry and hardness.

5.4. Multi – objective optimization using desirability and overlay plot

To achieve the desired output in AM, multi-objective optimization was performed by analyzing individual responses such as bead width, DOP, diffusion area, and microhardness using response surface models. The optimization targeted maximum bead width and height, minimum penetration and dilution, and higher hardness. During the optimization process, all process parameters were kept within their specified ranges. The DOP was minimized, while the other responses were maintained within their desired limits. Optimal conditions were determined based on the highest desirability values, ensuring a balanced trade-off among the multiple responses. The overlay plot, shown in Fig. 9. displays the predicted region satisfying all specified criteria. The optimal parameter combination was identified as a welding current of 150 A, a travel speed of 5 mm/s, and a shielding gas composition of 0-10% CO_2. Under these conditions, the process achieved a bead geometry with favorable characteristics and a corresponding microhardness of 180 HV.

5.5. Fabrication of WAAM structure based on optimized conditions

To validate the optimized process parameters, welding experiments were conducted under the recommended conditions. A robot was programmed using a teach pendant, as illustrated in Fig. 1. A multi-wall configuration was constructed by sequentially depositing layers using the optimized parameters. A dwell time of 120s was maintained between each layer to regulate thermal accumulation during the build process. This interval al-

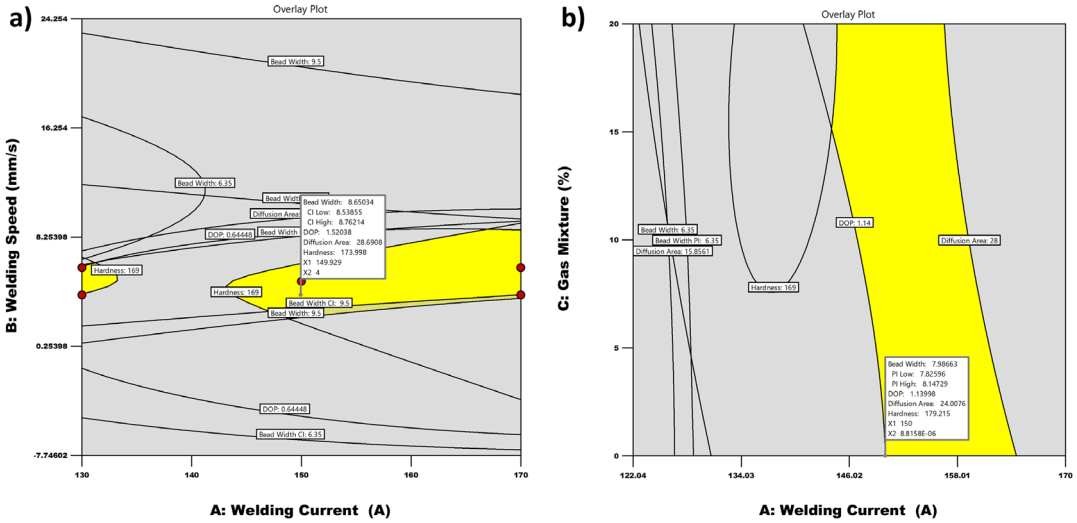

Fig. 9. Overlay plot-optimized parameter

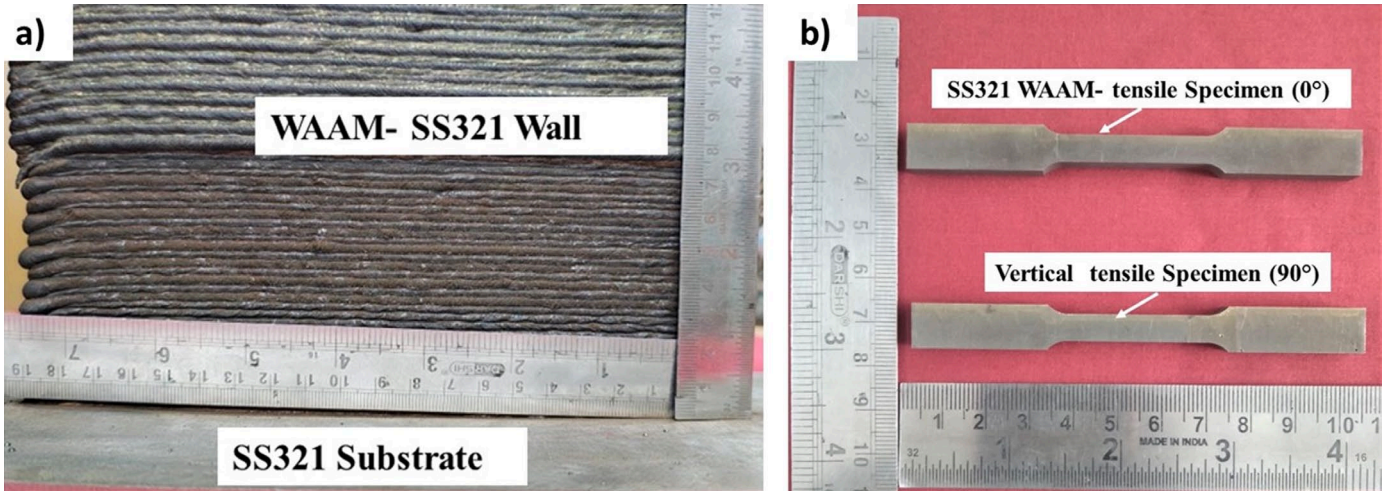

Fig. 10. (a) WAAM-printed SS321 thin wall, (b) tensile specimens extracted in different orientations from the SS321 wall

lowed for sufficient heat dissipation, thereby minimizing thermal gradients and enhancing both microstructural uniformity and mechanical performance [23,24,33].

The selected process parameters included a welding current of 150 A, a travel speed of 4 mm/s, and a shielding gas mixture of 98% Ar and 2% CO_2. The ER321 filler wire was deposited layer by layer to fabricate a wall with final dimensions of 200 mm × 120 mm × 8 mm on the SS321 substrate. Tensile specimens were extracted using a wire electrical discharge machine (WEDM) from various locations along the horizontal direction (0°) and vertical direction (90°) of the WAAM structure, in accordance with ASTM E8 standards, as shown in Fig. 10.

5.6. Tensile properties and SEM fractography of WAAM SS321 thin-wall structures

TABLE 6 details the tensile properties of WAAM-fabricated SS321 thin-wall specimens evaluated in horizontal (0°) and vertical (90°) deposition orientations. Uniaxial tensile tests were performed at ambient temperature using a 10 kN universal testing machine. Each value corresponds to a single specimen tested per orientation**;** therefore, standard deviation or standard error is not reported. The tests were conducted at a cross-head speed of 1 mm/min, corresponding to the standard strain rate for quasi-static tensile testing. The tensile properties are summarized below and graphically represented in Fig. 11. The WAAM SS321 specimens exhibit yield strength (YS) and UTS values that substantially surpass the ASTM A240/A240M-20a specifications for SS321, which are YS: 205 MPa, UTS: 515 MPa, and elongation: 40% [22].

Notably, the 0° (horizontal) specimens exhibited a slightly higher average ultimate tensile strength (UTS) of 594 ± 6 MPa and a comparable yield strength (YS) of 378 ± 7 MPa compared to the 90° (vertical) specimens, which recorded a UTS of 586 ± 6 MPa and a YS of 387 ± 5 MPa. The marginal reduction in tensile strength for the vertical orientation can be attributed to interlayer boundaries oriented perpendicular to the loading direction, which may serve as preferential sites for strain localization and micro-void initiation. In contrast, the horizontal orienta-

TABLE 6

Tensile results of various orientations of WAAM-fabricated SS321 structure

Materials	Build direction	YS (MPa) ± SD	Avg YS (MPa) ± SD	UTS (Mpa) ± SD	Avg UTS (MPa) ± SD	EL (%) ± SD	Avg EL (%) ± SD
SS321 – 0° (horizontal)	H1	372.07 ± 8	378.26 ± 7.2	590.19 ± 9	594.5 ± 6.1	42.44 ± 1	41.15 ± 1.8
	H2	380.32 ± 6		596.82 ± 5		40.63 ± 2	
	H3	382.38 ± 8		596.49 ± 4		40.37 ± 2	
SS321-90° (vertical)	V1	384.46 ± 6	386.53 ± 5.2	598.96 ± 8	586.0 ± 6.3	39.79 ± 3	39.47 ± 2.1
	V2	387.52 ± 5		586.21 ± 6		38.94 ± 2	
	V3	387.62 ± 5		588.12 ± 6		39.68 ± 1	

Note: H, horizontal direction; V, vertical direction; Avg, average; SD, Standard deviation; EL, Elongation

tion experiences loading along the deposition direction, where metallurgical continuity between successive layers promotes a more uniform stress distribution and enhanced load transfer. The horizontal specimens also demonstrated slightly greater ductility (41 ± 2%) than their vertical counterparts (39 ± 2%), highlighting anisotropic mechanical behavior governed by build orientation. Although WAAM-fabricated austenitic stainless steels typically exhibit higher tensile strength in the horizontal direction due to more uniform dendritic morphology and fewer interpass interfaces, the present study shows a reverse trend, with the vertical (90°) specimens exhibiting slightly higher YS and UTS values. This behavior can be attributed to repeated reheating cycles during vertical deposition, which generate interpass regions with coarser dendritic structures while simultaneously promoting strong metallurgical bonding between layers, thereby reducing micro-void initiation at interlayer boundaries and enhancing load-bearing capacity along the build direction. Comparable strengthening behavior in vertically oriented WAAM builds has been reported in recent studies on austenitic stainless steels [34,35].

To clarify the orientation-dependent mechanical response, additional optical and SEM images were included (Fig. 12(a)-(d). Optical micrographs of the cross-sections (Fig. 12(a)-(b) show that the 0° specimens exhibit equi-axed dendritic features aligned with the deposition direction, whereas the 90° specimens reveal interpass regions with fine coarser dendritic morphology resulting from repeated reheating. SEM fractography (Fig. 12(c)-(d) indicates ductile failure in both orientations: the 0° specimens display fine dimples and micro-void corresponding to higher ductility, while the 90° specimens show deeper fine dimples, confirming strong interlayer bonding. Overall, the WAAM-fabricated SS321 thin-wall structure achieved tensile properties that meet or exceed ASTM standard specifications for wrought SS321.

The SEM fractography, shown in Fig. 12, reveals uniformly distributed micro-voids and fine dimples on the fracture surfaces of both orientations, characteristic of ductile failure. The pronounced cup-and-cone morphology corroborates the high ductility observed in the tensile results, aligning well with the measured elongation values. The 0° specimen, exhibiting slightly higher elongation, showed more elongated dimples, whereas the 90° specimen, with marginally higher UTS, displayed deeper equiaxed dimples indicative of strong interlayer bonding. These findings confirm that WAAM-fabricated SS321 not only meets but exceeds ASTM standards, offering robust mechanical performance. The observed anisotropy highlights the influence of deposition direction on microstructural evolution and no secondary phase is observed near fracture surface, emphasizing the importance of optimizing WAAM process parameters for structural applications.

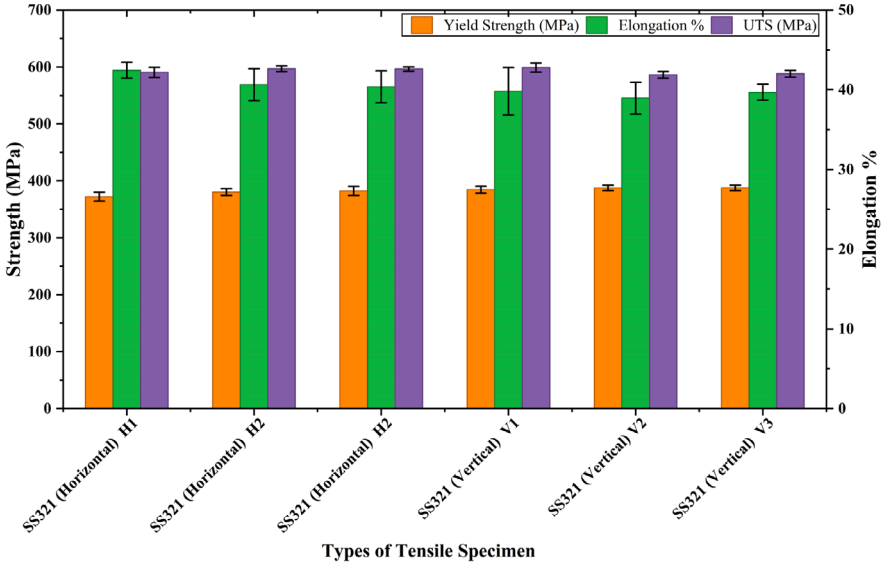

Fig. 11. Tensile properties of various orientations as deposited

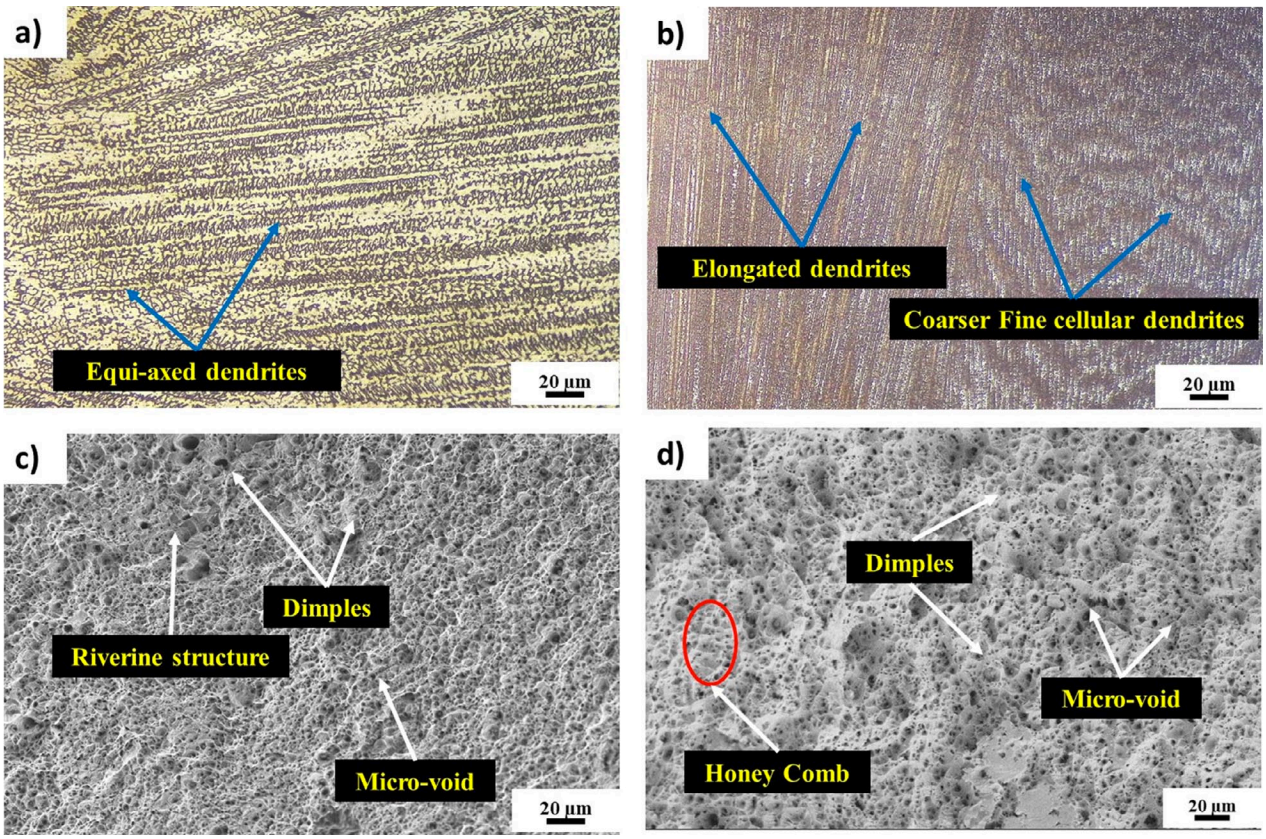

Fig. 12. Microstructural and SEM fractography analysis of WAAM-deposited SS321 thin-wall specimens

Furthermore, the average δ-ferrite fraction was estimated from optical micrographs to be approximately 6.0% in the horizontal specimens and 6.6% in the vertical specimens. Although hardness mapping was not performed for the thin-wall specimens, this slightly higher δ-ferrite content in the vertical specimens provides additional microstructural support for the observed orientation-dependent tensile response, consistent with literature reports that δ-ferrite content influences yield strength and hardness in WAAM-deposited austenitic stainless steels [22,34,35].

6. Conclusion

This study used optimization and prediction techniques to characterize SS321 material using the CMT-WAAM method, focusing on weld bead geometry and microhardness. RSM- CCD were applied to achieve optimization, and their results were to determine the most accurate model for predicting the output response of the CMT-WAAM process. The outcomes of this study are summarized below:

- The influence of argon and CO_2 gas mixtures was analyzed as one of the process parameters. The Ar + CO_2 compositions resulted in deeper penetration, comparable to that achieved with pure argon. However, microhardness, bead uniformity, and overall quality were found to be superior with 100% argon gas compositions.
- The RSM effectively identified optimal parameters for the CMT-based WAAM process applied to SS321 bead-on-plate weldments. The optimal parameters were found to be a welding current of 150 A, a travel speed of 4 mm/s, and a shielding gas of 100% argon. These conditions yielded optimal outcomes for bead width, DOP, and a microhardness value of 180 HV.
- The optimized parameters were validated through thin-wall fabrication. Tensile testing showed that the 0° (horizontal) specimen had an average YS of 378 ± 7 MPa, UTS of 595 ± 6 MPa, and elongation of 41 ± 2%, while the 90° (vertical) specimen exhibited an average YS of 387 ± 5 MPa, UTS of 586 ± 6 MPa, and elongation of 39 ± 2%. These results indicate slight anisotropy in mechanical behavior due to build orientation, reflecting the influence of microstructure and layer deposition.
- Optical micrographs showed that build orientation affects dendrite morphology, with 0° specimens exhibiting equiaxed dendrites and 90° specimens showing elongated, coarser cellular dendrites. SEM fractography revealed corresponding fracture features, including fine dimples and micro-voids in 0° specimens, and deeper dimples with the micro-voids in 90° specimens, reflecting orientation-dependent ductile fracture behavior.
- The optimized parameters were validated by fabricating a SS321 thin-wall structure using CMT-based WAAM. Tensile testing and SEM fractography confirmed adequate ductility and mechanical strength, comparable to those of wrought SS321 and in compliance with ASTM A240/A240M-20a standards.

Acknowledgment

The authors sincerely thank the Department of Robotics and Automation Engineering and the Centre of Excellence in Welding Engineering and Technology (CoEWT) at PSG College of Technology, Coimbatore, for providing the necessary facilities and technical support for this research. The authors also gratefully acknowledge the PSG College of Technology Research Fellowship for sponsoring and supporting this work.

REFERENCES

[1] M.F.G.M. Koizumi, FGM Activities in Japan. Compos. Part B Eng. **28** (1-2), 1-4 (1997).
DOI: https://doi.org/10.1016/S1359-8368(96)00016-9

[2] Rumman, D.A. Lewis, J.Y. Hascoet, J.S. Quinton, Laser Metal Deposition and Wire Arc Additive Manufacturing of Materials: An Overview. Arch. Metall. Mater. **64** (2), 467-473 (2019).
DOI: https://doi.org/10.24425/amm.2019.127561

[3] B. Wu, Z. Pan, D. Ding, D. Cuiuri, D. Li, H. Xu, J. Norrish, A Review of the Wire Arc Additive Manufacturing of Metals: Properties, Defects, and Quality Improvement. J. Manuf. Process **35**, 127-139 (2018).
DOI: https://doi.org/10.1016/j.jmapro.2018.08.001

[4] J. Jafari, T.H. Daneker, I. Gibson, Wire and Arc Additive Manufacturing: Opportunities and Challenges to Control the Quality and Accuracy of Manufactured Parts. Mater. Des. **202**, 109471 (2021).
DOI: https://doi.org/10.1016/j.matdes.2021.109471

[5] B.P. Nagasai, S. Malarvizhi, V. Balasubramanian, Mechanical Properties and Microstructural Characteristics of Wire Arc Additive Manufactured 308L Stainless Steel Cylindrical Components Made by Gas Metal Arc and Cold Metal Transfer Arc Welding Processes. J. Mater. Process. Technol. **307**, 117655 (2022).
DOI: https://doi.org/10.1016/j.jmatprotec.2022.117655.

[6] S. Selvi, A. Vishvaksenan, E. Rajasekar, Cold Metal Transfer (CMT) Technology – An Overview. Def. Technol. **14** (1), 28-44 (2018).
DOI: https://doi.org/10.1016/j.dt.2017.08.002

[7] A. Schierl, The CMT Process: A Revolution in Welding Technology. Weld. World **49** (1), 38(2005).

[8] V. Moura, A.Y. Kina, S.S.M. Tavares, L.D. Lima, F.B. Mainier, Influence of Stabilization Heat Treatments on Microstructure, Hardness, and Intergranular Corrosion Resistance of the AISI 321 Stainless Steel. J. Mater. Sci. **43** (2), 536-540 (2008).
DOI: https://doi.org/10.1007/s10853-007-1785-5

[9] X. Wang, Q. Hu, W. Liu, W. Yuan, X. Shen, F. Gao, D. Tang, Z. Hu, Microstructure and Corrosion Properties of Wire Arc Additively Manufactured Multi-Trace and Multilayer Stainless Steel 321. Metals **12** (6), 1039 (2022).
DOI: https://doi.org/10.3390/met12061039

[10] Z. Qiu, B. Wu, H. Zhu, Z. Wang, A. Hellier, Y. Ma, H. Li, O. Muransky, D. Wexler, Microstructure and Mechanical Properties of Wire Arc Additively Manufactured Hastelloy C276 Alloy. Mater. Des. **195**, 109007 (2020).
DOI: https://doi.org/10.1016/j.matdes.2020.109007

[11] M. Dinovitzer, X. Chen, J. Laliberte, X. Huang, H. Frei, Effect of Wire and Arc Additive Manufacturing (WAAM) Process Parameters on Bead Geometry and Microstructure. Addit. Manuf. **26**, 138-146 (2019).
DOI: https://doi.org/10.1016/j.addma.2018.12.020

[12] M. Yamaguchi, R. Komata, T. Furumoto, S. Abe, A. Hosokawa, Influence of Metal Transfer Behavior under Ar and CO_2 Shielding Gases on Geometry and Surface Roughness of Single and Multilayer Structures in GMAW-Based Wire Arc Additive Manufacturing of Mild Steel. Int. J. Adv. Manuf. Technol. **121**, 1-16 (2022).
DOI: https://doi.org/10.1007/s00170-022-09387-4

[13] G.P. Rajeev, M. Kamaraj, S.R. Bakshi, Effect of Correction Parameters on Deposition Characteristics in Cold Metal Transfer Welding. Mater. Manuf. Process. **34** (11), 1-12 (2019).
DOI: https://doi.org/10.1080/10426914.2019.1628260

[14] A.R. Pavan, N. Chandrasekar, B. Arivazhagan, S. Kumar, M. Vasudevan, Study of arc characteristics using varying shielding gas and optimization of activated-tig welding technique for thick AISI 316L (N) plates. CIRP J. Manuf. Sci. Technol. **35**, 675-690 (2021).
DOI: https://doi.org/10.1016/j.cirpj.2021.05.005

[15] S. Mohan Kumar, S. Sankarapandian, N.S. Shanmugam, Investigations on mechanical properties and microstructural examination of activated TIG-welded nuclear grade stainless steel. J. Braz. Soc. Mech. Sci. Eng. **42**, 1-21 (2020).
DOI: https://doi.org/10.1007/s40430-020-2230-5

[16] F. Kolahan, M. Heidari, A new approach for predicting and optimizing weld bead geometry in GMAW. Int. J. Mech. Syst. Sci. Eng. **2** (2), 138-142 (2010).

[17] P.S. Sivasakthivel, R. Sudhakaran, Modelling and optimisation of welding parameters for multiple objectives in pre-heated gas metal arc welding process using nature instigated algorithms, Australian Journal of Mechanical Engineering **18** (sup1), 76-87 (2018).
DOI: https://doi.org/10.1080/14484846.2018.1472721

[18] R. Narang, V. Maheshwari, P. Khanna, Prediction of bead geometry parameters in MIG welded stainless steel 409L plates by mathematical modelling. Mater. Today Proc. **44**, 900-908 (2021).
DOI: https://doi.org/10.1016/j.matpr.2020.10.795

[19] H. Lee, C. Ji, J. Yu, Effects of welding current and torch position parameters on bead geometry in cold metal transfer welding. J. Mech. Sci. Technol. **32**, 4335-4343 (2018).
DOI:https://doi.org/10.1007/s12206-018-0831-3

[20] C.V. Haden, G. Zeng, F.M. Carter III, C. Ruhl, B.A. Krick, D.G. Harlow, Wire and arc additive manufactured steel: tensile and wear properties. Addit. Manuf. 16, 115-123 (2017).
DOI: https://doi.org/10.1016/j.addma.2017.05.010

[21] D.T. Sarathchandra, M.J. Davidson, G. Visvanathan, Parameters effect on SS304 beads deposited by wire arc additive manufacturing. Mater. Manuf. Process. **35** (7), 852-858 (2020).
DOI: https://doi.org/10.1080/10426914.2020.1743852

[22] S.M. Kumar, A.R. Kannan, R. Pramod, N.S. Shanmugam, S.M. Muthu, V. Dhinakaran, Microstructure and high temperature performance of 321 SS wall manufactured through wire+arc additive manufacturing. Mater. Lett. **314**, 131913 (2022).
DOI: https://doi.org/10.1016/j.matlet.2022.131913

[23] K.S. Prakash, A.R. Kannan, R. Pramod, N.P. Kumar, N.S. Shanmugam, Microstructure, mechanical properties, and fracture toughness of SS 321 stainless steel manufactured using wire arc additive manufacturing. Trans. Indian Inst. Met. **76** (2), 537-544 (2023).
DOI: https://doi.org/10.1007/s12666-022-02713-3

[24] V. HM, R.N. Rao, M. Maiya, P. Kumar, N. Gupta, K.K. Saxena, V. Vijayan, Effects of arc current and travel speed on the processing of stainless steel via wire arc additive manufacturing (WAAM) process. J. Adhes. Sci. Technol. **38** (12), 2222-2239 (2024).
DOI: https://doi.org/10.1080/01694243.2023.2289770

[25] R. Roshan, A. Kumar Naik, K. Kumar Saxena, K.S. Arora, N. Shajan, V. Msomi, H. Mehdi, Effect of welding speed and wire feed rate on arc characteristics, weld bead, and microstructure in standard and pulsed gas metal arc welding. J. Adhes. Sci. Technol. **37** (23), 3297-3314 (2023).
DOI: https://doi.org/10.1080/01694243.2023.2192314

[26] T.E. Abioye, O.E. Ariwoola, T.I. Ogedengbe, P.K. Farayibi, O.O. Gbadeyan, Effects of welding speed on the microstructure and corrosion behavior of dissimilar gas metal arc weld joints of AISI 304 stainless steel and low carbon steel. Mater. Today Proc. **17**, 871-877 (2019).
DOI: https://doi.org/10.1016/j.matpr.2019.06.383

[27] S. Roy, B. Silwal, A. Nycz, M. Noakes, E. Cakmak, P. Nandwana, Y. Yamamoto, Investigating the effect of different shielding gas mixtures on microstructure and mechanical properties of 410 stainless steel fabricated via large scale additive manufacturing. Addit. Manuf. **38**, 101821 (2021).
DOI: https://doi.org/10.1016/j.addma.2020.101821

[28] F. Marefat, A. Kapil, S.A. Banaee, P. Van Rymenant, A. Sharma, Evaluating shielding gas-filler wire interaction in bi-metallic wire arc additive manufacturing (WAAM) of creep resistant steel-stainless steel for improved process stability and build quality. J. Manuf. Process. **88**, 110-124 (2023).
DOI: https://doi.org/10.1016/j.jmapro.2023.01.046

[29] M.T. Liao, W.J. Chen, The effect of shielding-gas compositions on the microstructure and mechanical properties of stainless steel weldments. Mater. Chem. Phys. **55** (2), 145-151 (1998).
DOI: https://doi.org/10.1016/S0254-0584(98)00134-5

[30] J.A. Brooks, A.W. Thompson, Microstructural development and solidification cracking susceptibility of austenitic stainless steel welds. Int. Mater. Rev. **36** (1), 16-44 (1991).
DOI: https://doi.org/10.1179/imr.1991.36.1.16

[31] M. Ebrahimnia, M. Goodarzi, M. Nouri, M. Sheikhi, Study of the effect of shielding gas composition on the mechanical weld properties of steel ST 37-2 in gas metal arc welding. Mater. Des. **30** (9), 3891-3895 (2009).
DOI: https://doi.org/10.1016/j.matdes.2009.03.031

[32] S. Kumar Jain, Q. Murtaza, P. Singh, CMT assisted wire arc additive manufacturing of SS316L: fabrication characterization and fractography. Arch. Metall. Mater. **70** (1), 147–153 (2025).
DOI: https://doi.org/10.24425/amm.2025.152528

[33] ASTM International, A240/A240M-20a Standard Specification for Chromium and Chromium-Nickel Stainless Steel Plate, Sheet, and Strip for Pressure Vessels and for General Applications. ASTM Int., West Conshohocken, PA (2020).
DOI: https://doi.org/10.1520/A0240_A0240M-20A

[34] Kun Li, Wen Chen, Na Gong, Huayan Pu, Jun Luo, David Z. Zhang, Lawrence E. Murr, A critical review on wire-arc directed energy deposition of high-performance steels. Journal of Materials Research and Technology **24**, 9369-9412 (2023).
DOI: https://doi.org/10.1016/j.jmrt.2023.05.163

[35] A Kannan,. N. Rajesh, K. Siva Shanmugam, Sanjeeviprakash, Yasam Palguna, Rajesh Korla, Wonjoo Lee, YuHyeong Jeong, Jonghun Yoon. Room and high-temperature tensile properties of austenitic stainless steel 321 fabricated by wire arc additive manufacturing. Journal of Materials Research and Technology **36**, 3996-4004 (2025).
DOI: https://doi.org/10.1016/j.jmrt.2025.04.084